Supplementary Information

Organocatalytic Iminium-Assisted Asymmetric B(sp²)-to-B(sp³) Transformation

Yingling Nong,[1,†] Sai V. C. Vummaleti,[2,†] Yili Zhang,[3] Yingzhu Sun,[4] Lingzhu Chen,[1] Zhichao Jin,[1,]* Huicai Huang,[3,]* Erhong Hao,[4,]* Xinglong Zhang[2,5,]* and Yonggui Robin Chi[1,6,]*

[1]State Key Laboratory of Green Pesticide, Guizhou University, Guiyang, 550025, China.

[2]Institute of High Performance Computing, Agency for Science, Technology and Research (A*STAR) Singapore, 138632, Singapore.

[3]Key Laboratory of Chinese Medicinal Resource from Lingnan, Ministry of Education, School of Pharmaceutical Sciences, Guangzhou University of Chinese Medicine, Guangzhou, 510006, China.

[4]Key Laboratory of Functional Molecular Solids, Ministry of Education, School of Chemistry and Materials Science, Anhui Normal University, Wuhu, Anhui, 241002, China.

[5]Department of Chemistry, The Chinese University of Hong Kong, Shatin, New Territories, Hong Kong, 999077, China.

[6]School of Chemistry, Chemical Engineering, and Biotechnology, Nanyang Technological University, Singapore, 637371, Singapore.

[†]These authors contributed equally.

*Email: Zhichao Jin, zcjin@gzu.edu.cn; Huicai Huang, huanghc@gzucm.edu.cn; Erhong Hao, haoehong@ahnu.edu.cn; Xinglong Zhang, xinglong.zhang@cuhk.edu.hk; Yonggui Robin Chi, robinchi@ntu.edu.sg

Contents

VI. DFT study

1. Computational methods for mechanism studies.

Geometry optimizations in the gas phase were initially carried out using global hybrid functional M06-2X[5] with Karlsruhe-family basis set of double-ζ valence def2-SVP[6,7] for all atoms as implemented in *Gaussian 16* rev. A.03.[8] Minima and transition structures on the potential energy surface (PES) were confirmed as such by harmonic frequency analysis, showing respectively zero and one imaginary frequency, at the same level of theory.

Single point (SP) corrections were performed using M06-2X functional and def2-TZVP[6] basis set for all atoms. The implicit SMD continuum solvation model[9] was used to account for the solvent effects of diethylether (DEE) on the overall free energy PES. Gibbs energies were evaluated at the room temperature, as was used in the experiments, using a quasi-RRHO treatment of vibrational entropies.[10,11] Vibrational entropies of frequencies below 100 cm^{-1} were obtained according to a free rotor description, using a smooth damping function to interpolate between the two limiting descriptions. The free energies were further corrected using standard concentration of 1 mol/L, which was used in solvation calculations. SMD(DEE)-M06-2X/def2-TZVP//M06-2X/def2-SVP Gibbs energies are given and quoted in kcal mol^{-1} throughout. *Unless otherwise stated, these solvent-corrected values are used for discussion throughout the main text and in this supporting information.*

For photochemical properties study of compounds **3a** and **3j**, geometries were optimized at the level of theory (M06-2X/def2-SVP) using Gaussian 16 rev. A.03. Subsequently, the time-dependent DFT (TD-DFT) calculations were carried out on the gas-phase optimized geometries using ORCA 5.0.4,[12] with CAM-B3LYP[13] functionals and def2-TZVPD basis sets[6,7] for all atoms, in implicit toluene solvent. For the TD-DFT calculations, five singlet and five triplet excited states were computed (*nroots* = 5) to adequately capture the lowest-lying electronic excitations relevant to photophysical processes. Spin–orbit coupling (SOC) matrix elements between the singlet and triplet manifolds were subsequently evaluated using the *doSOC* keyword to assess the efficiency of possible intersystem crossing (ISC) pathways. CAM-B3LYP functional was chosen for its robust performance in TD-DFT studies.[14]

Non-covalent interactions (NCIs) and molecular orbitals (MOs) were analyzed using NCIPLOT[15] calculations. The *.wfn* files for NCIPLOT were generated at M06-2X/def2-SVP[6,7] level of theory. NCI indices calculated with NCIPLOT were visualized at a gradient isosurface value of *s = 0.5* au. These are colored according to the sign of the second eigenvalue (λ_2) of the Laplacian of the density ($\nabla^2\rho$) over the

range of –0.1 (blue = attractive) to +0.1 (red = repulsive). All molecular structures were visualized using *PyMOL* software.[16]

2. Model reaction.

For this study, we select the model reaction depicted in Scheme S1 for mechanistic studies using DFT modeling.
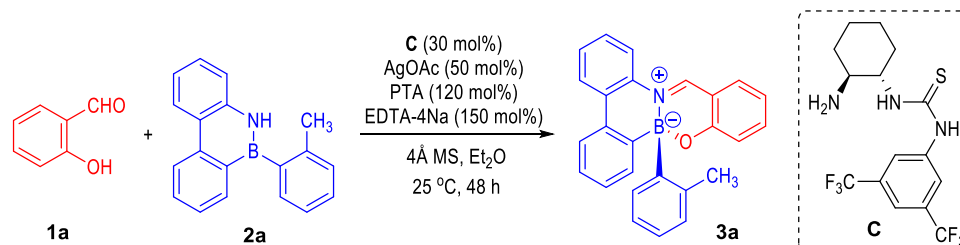
Scheme S1. Model reaction used for DFT based mechanistic studies.

3. Conformational considerations.

We first obtained the DFT optimized (M06-2X/def2-SVP level of theory) TSs for the studied reaction mechanism, which consists of five TSs, **TS1_*Re***, **TS1_*Si***, **TS2**, **TS2′**, and **TS3**. Subsequently, we utilized these DFT-optimized TS structures as input to conduct thorough constrained conformational sampling using the *crest* program, aiming to identify the corresponding most stable TS conformers. From the sampling, we extracted the five lowest energy TS conformers (optimized at the *xtb* level), resulting in a total 25 conformers. These *xtb*-optimized conformers were then reoptimized at the DFT M06-2X/def2-SVP level of theory. Note that for **TS1_*Si***, we have only succeeded in obtaining 3 optimized TS structures, resulting in a total 23 stable conformers. The DFT-optimized lowest energy TS conformer for each step was used for all discussions. Note that the initial guess structures for **TS2_*minor*** and **TS2′_*minor*** were constructed from the corresponding DFT-optimized lowest-energy conformers **TS2** and **TS2′**, respectively.

The most stable conformer for complex I, which is the resting state of the catalytic cycle and substrate **2a** were also located by DFT-optimizing the 5 lowest xTB energy structures and taking the most stable one.

4. Relative stabilities of imine form of intermediate I and its enone form.

Our calculations suggest that the reaction starts with the condensation of substrate **1a** with catalyst **C** to form the stable chiral imine intermediate **I**, with the release of one water molecule, Figure 3. This step is exergonic, with **I** lying at -3.8 kcal mol^{-1}. Notably, the *ortho*-quinone methide (*o*-QM)[17] intermediate, **I_enone** is 4.1 kcal mol^{-1} less

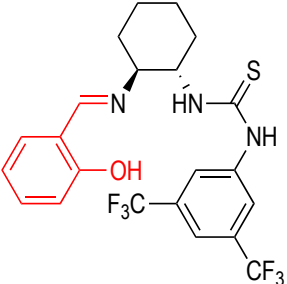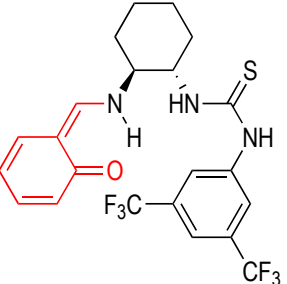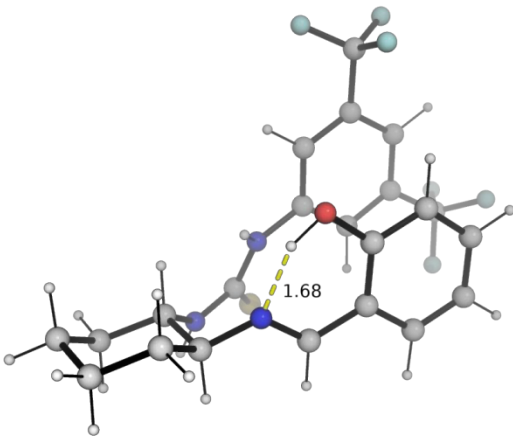stable (Figure S6). This is perhaps unsurprising as this form disrupts the aromaticity of the phenyl ring.
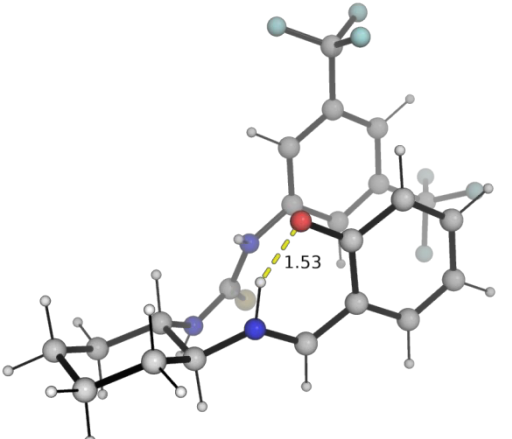
I	I_enone
ΔG = -3.8 kcal mol^{-1}	$\Delta\Delta G^{\ddagger}$ = 0.3 kcal mol^{-1}

Figure S6. DFT optimized geometries of intermediate **I** and its enone form, **I_enone**.

5. DFT geometries of the enantio-inducing TS structures.

From a structural perspective, **TS1_Re** represents an early transition state with a B–O bond length of 2.26 Å, while **TS1_Si** corresponds to a later transition state featuring a shorter B–O distance of 1.94 Å (Fig. S7) Our analysis reveals that **TS1_Re** is energetically favored over **TS1_Si**, primarily due to stronger non-covalent interactions such as π–π and C–H···π interactions (Fig. S7).
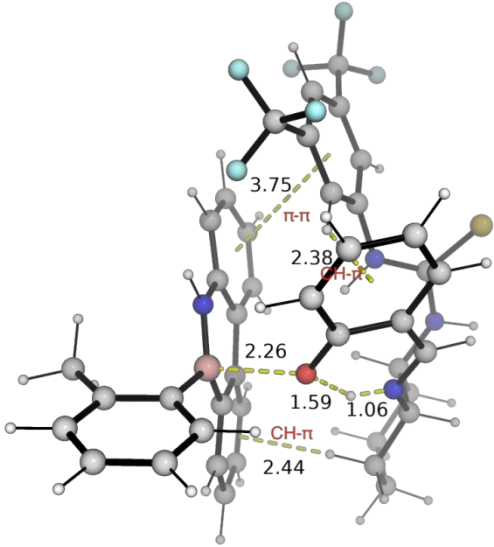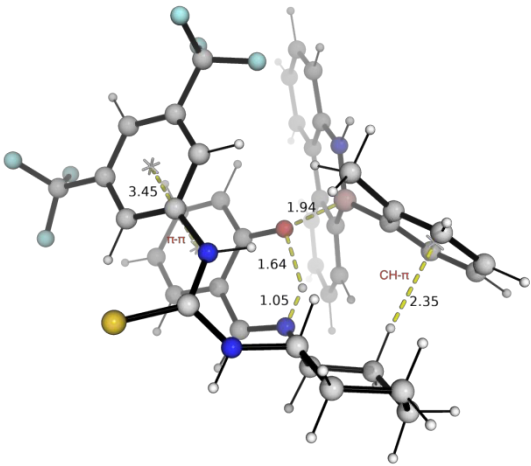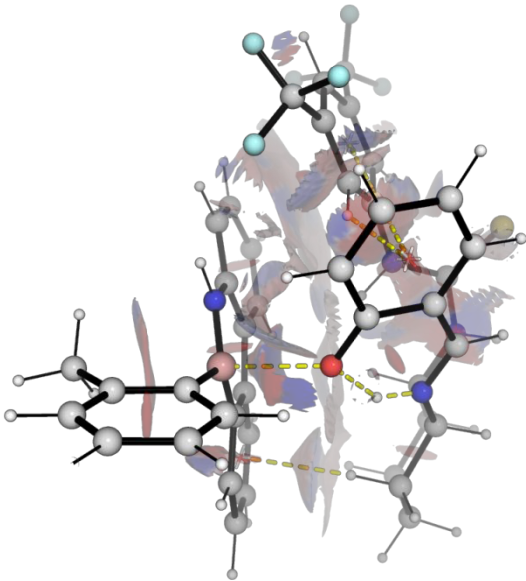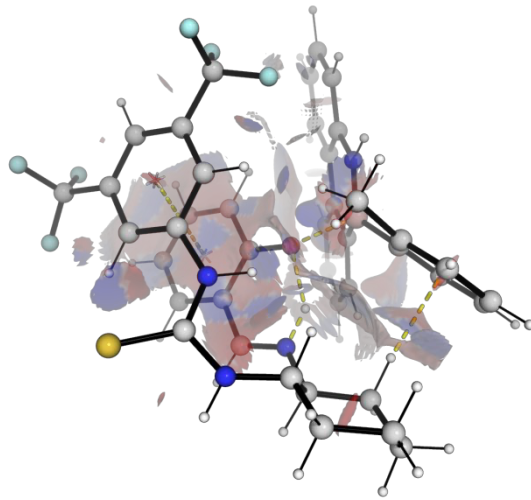
TS1_*Re*	TS1_*Si*
$\Delta\Delta G^{\ddagger}$ = 0.0 kcal mol^{-1}	$\Delta\Delta G^{\ddagger}$ = 1.9 kcal mol^{-1}

TS1_*Re*	TS1_*Si*
$\Delta\Delta G^{\ddagger}$ = 0.0 kcal mol^{-1}	$\Delta\Delta G^{\ddagger}$ = 1.9 kcal mol^{-1}

Figure S7. DFT optimized geometries of the enantio-determining TS structure (**TS1**), representing both *(Re)*- and the *(Si)*-face attacks by the OH group on **I** at the B(sp^2) center of **2a**, and the corresponding NCI plots, for the studied reaction mechanism. Key bond distances are given in Å. Activation barriers are given in kcal mol^{-1}, relative to

the lowest activation barrier. Gibbs energies were computed at SMD(DEE)-M06-2X/def2-TZVP//M06-2X/def2-SVP level of theory.

6. Enantio-determining intramolecular aminal formation step via stereoselective ring closure.

The intramolecular aminal formation reaction between the iminium ion moiety and the $N(sp^3)$ atom in **III**, via **TS2**, forms the stereoselective cyclic intermediate **IV** (see Figure 3 in the main text). The calculated TS barriers suggest that the $N(sp^3)$ atom preferentially attacks the carbon center of iminium ion moiety in **III** from the (*Re*)-face via **TS2** (barrier of 10.5 kcal mol^{-1} from **I**), which is 4.9 kcal mol^{-1} lower than the barrier from the (*Si*)-face via **TS2'** (barrier of 15.4 kcal mol^{-1}), Figure S8. Alternatively, along the pathway originating from **TS1_*Si*** and leading to the minor product, the corresponding TS2 structures (**TS2_*minor*** and **TS2'_*minor***) reveal that the lowest energy **TS2_*minor*** (21.7 kcal mol^{-1}) lies 2.8 kcal mol^{-1} higher than the corresponding **TS2** (18.9 kcal mol^{-1}) leading to the major product **3a**, Figure S8. While **TS1** serves as the enantio-inducing transition state, favoring the pathway leading to **3a** via **TS1_*Re*** over **TS1_*Si*** by 1.9 kcal mol^{-1}, the subsequent cyclization step (**III** → **IV**) via **TS2** is the enantio-determining step, with **TS2** favored over **TS2_*minor*** by 2.8 kcal mol^{-1}, thereby reinforcing the kinetic preference for enantioselective formation of product **3a**. From a thermodynamic perspective, intermediate **IV** (3.4 kcal mol^{-1} above **III**) is more stable by 7.2 kcal mol^{-1} than **IV'** (10.6 kcal mol^{-1} above **III**) formed via **TS2'**, Figure S9. Most importantly, from **IV'**, following the intramolecular proton transfer, the C–N bond dissociation step proceeds through a TS characterized by B–N bond cleavage, leading to ring-opening, curtailing the formation of the desired product **3a**. This is because, as the C–N(catalyst) bond breaks, it forms the C=N bond with *E* stereochemistry in **IV**, with the green H atom (Figure S9) *trans* to B atom, thus outside of the ring system, whereas in **IV'**, as the C–N(catalyst) bond breaks, it forms the C=N bond with *Z* stereochemistry with the green H atom (Figure S9) *cis* to B atom, thus placing it inside of the ring system, distorting the ring and causing B–N bond to break.
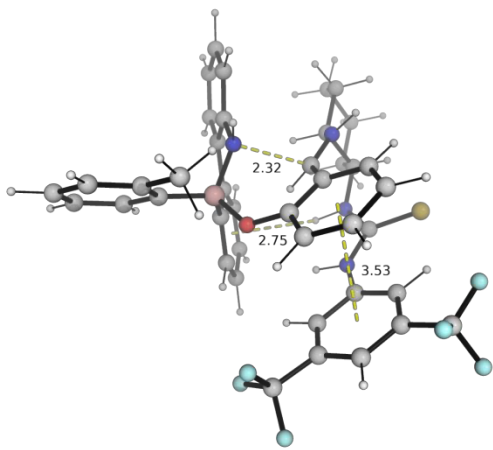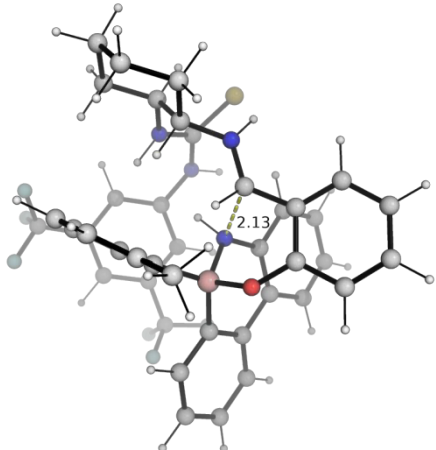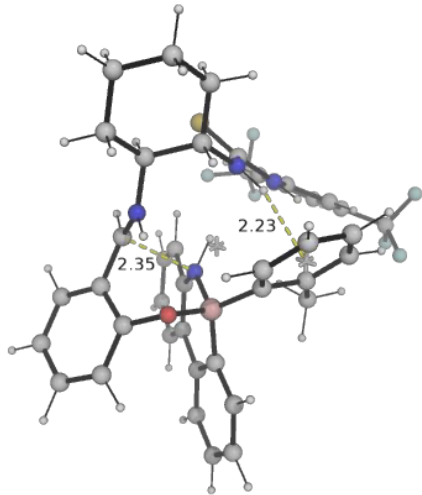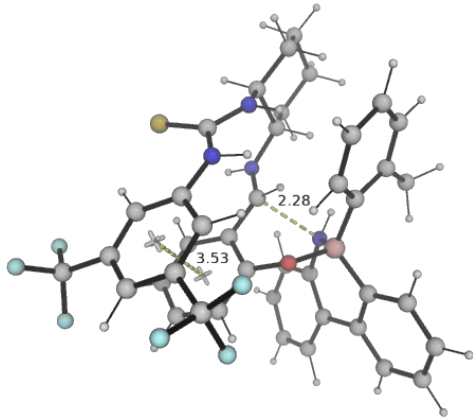
TS2	TS2′
$\Delta\Delta G^{\ddagger} = 0.0$ kcal mol^{-1}	$\Delta\Delta G^{\ddagger} = 4.9$ kcal mol^{-1}
TS2_minor	**TS2′_minor**
$\Delta\Delta G^{\ddagger} = 2.8$ kcal mol^{-1}	$\Delta\Delta G^{\ddagger} = 3.6$ kcal mol^{-1}

Figure S8. DFT-optimized geometries of the enantio- and rate-determining transition state **TS2**, leading to the major product 3a, and the less favorable TS structure, **TS2_minor**, associated with the minor pathway. The corresponding higher-energy isomers **TS2′** and **TS2′_minor** are also shown. Key bond distances are given in Å. Activation barriers are given in kcal mol^{-1}, relative to the lowest activation barrier. Gibbs energies were computed at SMD(DEE)-M06-2X/def2-TZVP//M06-2X/def2-SVP level of theory.
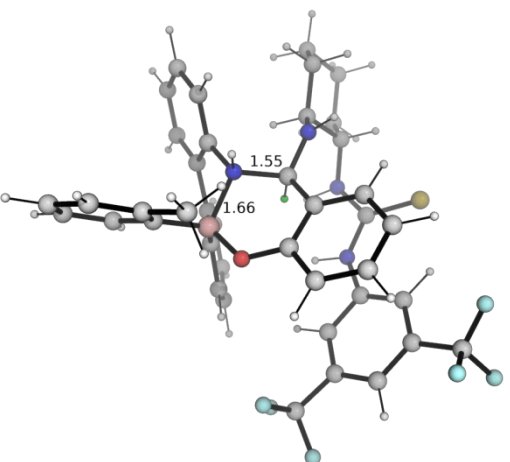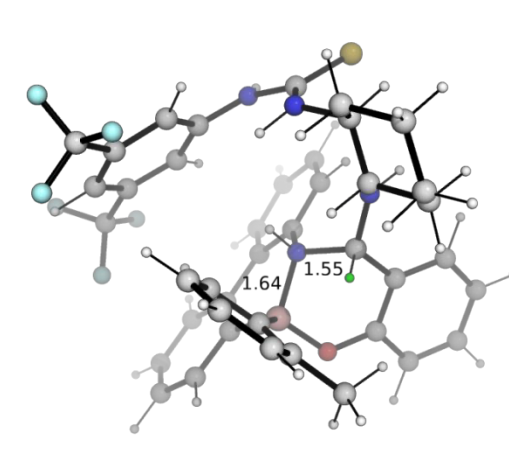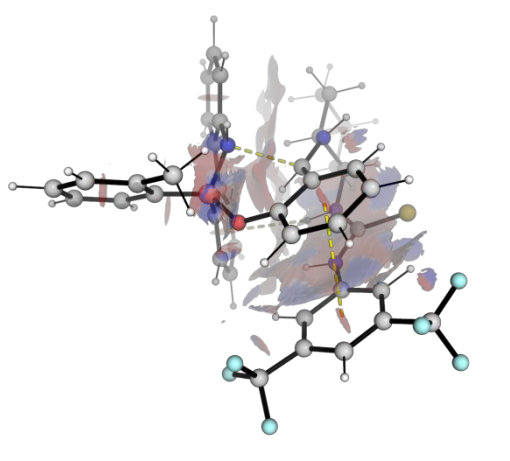
IV	IV′
ΔΔG = 0.0 kcal mol⁻¹	ΔΔG = 7.2 kcal mol⁻¹

Figure S9. DFT optimized geometries of the cyclic intermediate **IV** and its less stable stereoisomer, **IV′**. Key bond distance is given in Å. Gibbs energies were computed at SMD(DEE)-M06-2X/def2-TZVP//M06-2X/def2-SVP level of theory.

TS2	TS2′
ΔΔG‡ = 0.0 kcal mol⁻¹	ΔΔG‡ = 4.9 kcal mol⁻¹
TS2_*minor*	**TS2′_*minor***
ΔΔG‡ = 2.8 kcal mol⁻¹	ΔΔG‡ = 3.6 kcal mol⁻¹

Figure S10. NCI plots of the enantio- and rate-determining transition state **TS2** leading to major product **3a**, its less stable isomer **TS2′**, and the less favorable transition state **TS2_*minor*** on the minor pathway, along with its less stable isomer **TS2′_*minor***.

TS3
$\Delta G^{\ddagger} = 21.1$ kcal mol^{-1}
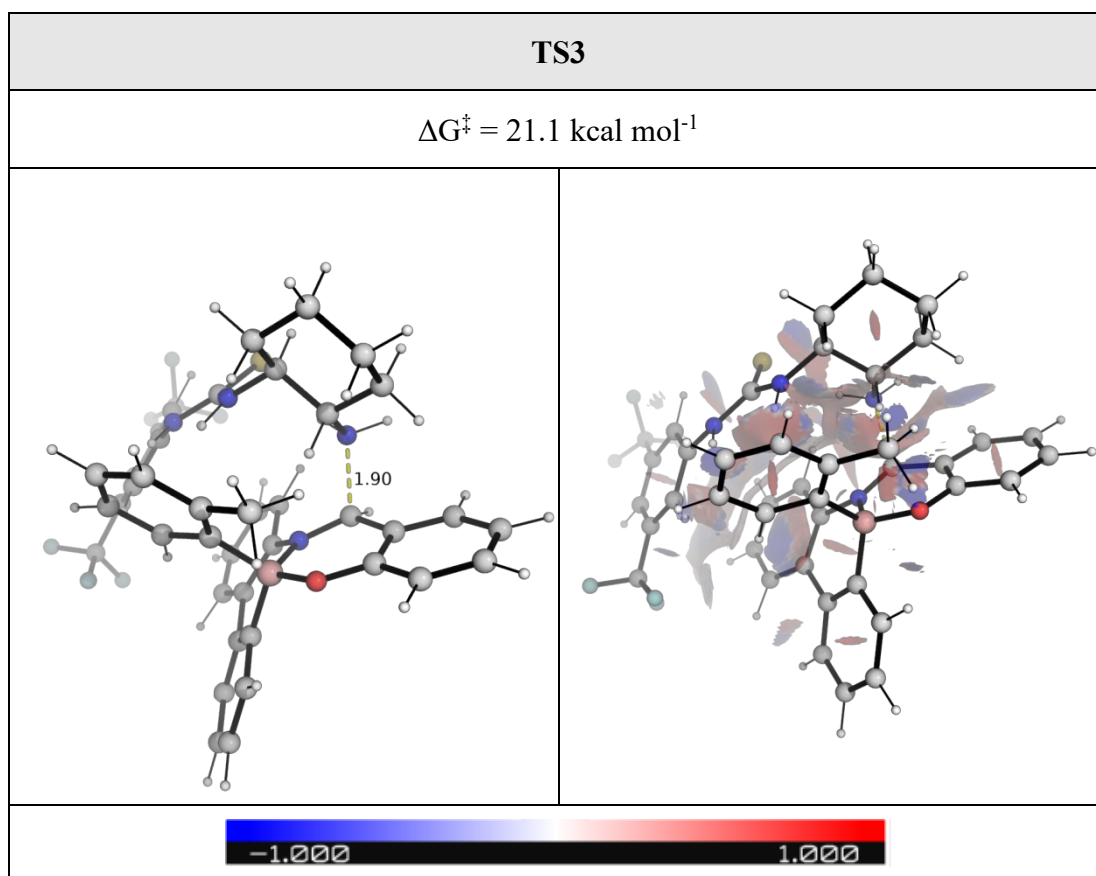
Figure S11. DFT optimized geometry of the C–NH$_2$ bond dissociation TS, **TS3**, and the corresponding NCI plot. Key bond distances are given in Å. Activation barriers are

given in kcal mol^{-1}. Gibbs energies were computed at SMD(DEE)-M06-2X/def2-TZVP//M06-2X/def2-SVP level of theory.

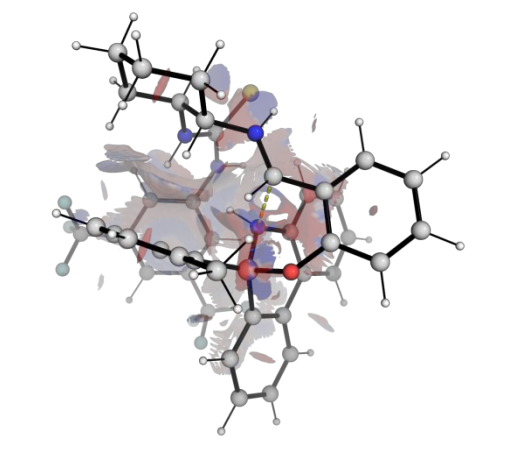## 7. Distortion-interaction Analysis for enantio-inducing and enantio-determining TSs.

Distortion-interaction analysis is applied to key TSs (**TS1** and **TS2**) to discern the factors affecting enantioselectivity. The transition state structures are decomposed by dividing the chiral imine intermediate **I**, and boron substrate **2a** as components. Single point calculations with SMD (diethylether) solvent correction were applied performed at M06-2X/def2-TZVP level of theory to obtain distortion and interaction energies. The distortion energy is given by:

$$E_{dist} = E_{TS,frag1} + E_{TS,frag2} - (E_{eq,frag1} + E_{eq,frag2})$$

where *TS,frag1,2* represent individual fragments in their distorted transition state geometries; and *eq,frag1,2* represent individual fragments in their optimized, equilibrium ground-state geometries; the interaction energy is given by:

$$E_{int} = E_{TS} - (E_{TS,frag1} + E_{TS,frag2})$$

which accounts for the stabilizing interactions (e.g., electrostatic, orbital, dispersion) between the distorted fragments in the TS.

Thus, the total activation energy is given by:

$$\Delta E^{\ddagger} = E_{dist} + E_{int.}$$

Note that this single point activation energy and the activation energy differences $\Delta\Delta E^{\ddagger}$ between the TSs (**TS1_Re** vs. **TS1_Si**, and **TS2** vs. **TS2_minor**) may be different from the Gibbs energy differences $\Delta\Delta G^{\ddagger}$ that is computed fully (including vibrational frequencies analysis) at SMD (diethylether)-M06-2X/def2-TZVP//M06-2X/def2-SVP level of theory.

This analysis gives a $\Delta\Delta E^{\ddagger}$ (**TS1**) of 1.1 kcal mol^{-1} in favor of **TS1_Re** over **TS1_Si**. Although **TS1_Re** exhibits a lower interaction energy (**E**$_{int}$) by 1.5 kcal mol^{-1}, this is outweighed by its distortion energy (**E**$_{dist}$), which is 2.6 kcal mol^{-1} lower than **TS1_Si**, Table S6. Similarly, the $\Delta\Delta E^{\ddagger}$ (**TS**) is 3.3 kcal mol^{-1} in favor of **TS2** relative to **TS2_minor**, primarily due to a significantly more stabilizing **E**$_{int}$ (–67.1 kcal mol^{-1} for **TS2** vs. –57.6 kcal mol^{-1} for **TS2_minor**). While **TS2** displays a slightly higher **E**$_{dist}$

(73.0 kcal mol^{-1} vs. 66.8 kcal mol^{-1}), which is more than compensated by its favorable interaction energy, resulting in a lower overall $\Delta E^\ddagger$ (5.9 kcal mol^{-1} vs. 9.2 kcal mol^{-1}) and making **TS2** the more favorable transition state, Table S6.

Table S6. Distortion-interaction analysis.

Transition State	$\Delta E^\ddagger$	E_{dist}	E_{int}
TS1_*Re*	0.7	13.6	-12.9
TS1_*Si*	1.8	16.2	-14.4
TS2	5.9	73.0	-67.1
TS2_*minor*	9.2	66.8	-57.6

8. Optimized structures and raw energies.

Geometries of all optimized structures (in .xyz format with their associated energy in Hartrees) are included in a separate folder named *DFT_optimized_structures*. All these data have been deposited and uploaded to https://zenodo.org/records/17047909 (DOI: 10.5281/zenodo.17047909).

Absolute values (in Hartrees) for SCF energy, zero-point vibrational energy (ZPE), enthalpy and quasi-harmonic Gibbs free energy (at 298.15K) for gas-phase M06-2X/def2-SVP optimized structures are given below. Single point corrections in SMD diethylether using M06-2X/def2-TZVP functional are also included.

Structure	E/au	ZPE/au	H/au	T.S/au	qh-G/au	SP M06-2X/def2-TZVP
1a	-420.321783	0.11649	-420.197445	0.036091	-420.233523	-420.809312
D	-1741.747131	0.323435	-1741.399592	0.078115	-1741.471525	-1743.454192
I_enone	-2085.749531	0.414707	-2085.305413	0.087053	-2085.386459	-2087.836942
H$_2$O	-76.323214	0.021594	-76.29784	0.018411	-76.316251	-76.432252
I_c1	-2085.760887	0.415805	-2085.315646	0.087453	-2085.396832	-2087.844486
I_c2	-2085.760887	0.415806	-2085.315646	0.087454	-2085.396832	-2087.844484

I_c3	-2085.758354	0.416253	-2085.312639	0.087743	-2085.394018	-2087.84227
I_c4	-2085.758354	0.416255	-2085.312637	0.087738	-2085.394013	-2087.842271
I_c5	-2085.758354	0.416253	-2085.312639	0.087737	-2085.394015	-2087.842269
2a_c1	-812.425851	0.30441	-812.104223	0.058826	-812.160641	-813.3269004
2a_c2	-812.425851	0.30441	-812.104224	0.058824	-812.16064	-813.3269004
2a_c3	-812.42585	0.304412	-812.104223	0.05882	-812.160637	-813.3269014
2a_c4	-812.425199	0.304469	-812.103516	0.059157	-812.160098	-813.3266408
2a_c5	-812.425199	0.304469	-812.103516	0.059155	-812.160097	-813.3266404
II	-2898.202119	0.720485	-2897.434159	0.127914	-2897.5500	-2901.173716
TS1_Re_c1	-2898.199446	0.719938	-2897.432976	0.124379	-2897.546591	-2901.170314
TS1_Re_c2	-2898.199445	0.719933	-2897.432972	0.124379	-2897.546592	-2901.170306
TS1_Re_c3	-2898.199446	0.719937	-2897.432977	0.124362	-2897.546584	-2901.170306
TS1_Re_c4	-2898.199446	0.719935	-2897.432979	0.124355	-2897.546583	-2901.170306
TS1_Re_c5	-2898.199446	0.719936	-2897.432979	0.124356	-2897.546583	-2901.170306
TS1_Si_c1	-2898.19467	0.720694	-2897.42762	0.123024	-2897.540514	-2901.168599
TS1_Si_c2	-2898.19348	0.721135	-2897.42583	0.125003	-2897.539631	-2901.16642
TS1_Si_c3	-2898.19348	0.721142	-2897.42582	0.124996	-2897.539621	-2901.16642
III	-2898.20945	0.722154	-2897.4409	0.122781	-2897.553814	-2901.178304
TS2_c1	-2898.19458	0.722442	-2897.42625	0.12291	-2897.538522	-2901.161974
TS2_c2	-2898.19377	0.722494	-2897.42539	0.12283	-2897.537639	-2901.161648
TS2_c3	-2898.19377	0.722491	-2897.4254	0.122808	-2897.537631	-2901.16165
TS2_c4	-2898.19377	0.722493	-2897.4254	0.122806	-2897.537629	-2901.16165
TS2_c5	-2898.19377	0.722493	-2897.4254	0.1228	-2897.537626	-2901.161649
TS2′_c1	-2898.19036	0.722752	-2897.42207	0.120051	-2897.532838	-2901.155607
TS2′_c2	-2898.19036	0.722782	-2897.42204	0.120041	-2897.532802	-2901.155577

TS2′_c3	-2898.19036	0.722801	-2897.42202	0.120041	-2897.532778	-2901.15555
TS2′_c4	-2898.19036	0.722807	-2897.42202	0.120032	-2897.532769	-2901.155545
TS2′_c5	-2898.18447	0.722264	-2897.41653	0.120606	-2897.52774	-2901.151967
TS2_minor	-2898.18916	0.722305	-2897.42087	0.124072	-2897.533861	-2901.156762
TS2′_minor	-2898.18483	0.721802	-2897.41702	0.12274	-2897.529323	-2901.155678
IV	-2898.21133	0.72486	-2897.4405	0.12264	-2897.552712	-2901.175781
IV′	-2898.20061	0.725377	-2897.42952	0.122201	-2897.541301	-2901.165142
V	-2898.20717	0.725542	-2897.43625	0.119147	-2897.546736	-2901.17221
TS3_c1	-2898.20475	0.724306	-2897.43535	0.118079	-2897.545115	-2901.168097
TS3_c2	-2898.20475	0.724306	-2897.43535	0.11808	-2897.545116	-2901.168098
TS3_c3	-2898.20475	0.724306	-2897.43535	0.118081	-2897.545116	-2901.168097
TS3_c4	-2898.20475	0.724306	-2897.43535	0.118079	-2897.545115	-2901.168097
TS3_c5	-2898.20183	0.723844	-2897.43279	0.118309	-2897.542578	-2901.167096
VI	-2898.22053	0.722673	-2897.45121	0.123384	-2897.564574	-2901.186254
3a-AgOAc	-1531.60831	0.448023	-1531.12954	0.092539	-1531.214161	-1533.167473
3a	-1156.42297	0.396106	-1156.00424	0.069953	-1156.07091	-1157.707986
3j	-1195.69011	0.424141	-1195.24176	0.073199	-1195.311515	-1197.018903

9. Full reference for Gaussian software:

Gaussian 16, Revision A.03, Frisch, M. J.; Trucks, G. W.; Schlegel, H. B.; Scuseria, G. E.; Robb, M. A.; Cheeseman, J. R.; Scalmani, G.; Barone, V.; Mennucci, B.; Petersson, G. A.; Nakatsuji, H.; Caricato, M.; Li, X.; Hratchian, H. P.; Izmaylov, A. F.; Bloino, J.; Zheng, G.; Sonnenberg, J. L.; Hada, M.; Ehara, M.; Toyota, K.; Fukuda, R.; Hasegawa, J.; Ishida, M.; Nakajima, T.; Honda, Y.; Kitao, O.; Nakai, H.; Vreven, T.; Montgomery Jr., J. A.; Peralta, J. E.; Ogliaro, F.; Bearpark, M.; Heyd, J. J.; Brothers, E.; Kudin, K. N.; Staroverov, V. N.; Kobayashi, R.; Normand, J.; Raghavachari, K.; Rendell, A.; Burant, J. C.; Iyengar, S. S.; Tomasi, J.; Cossi, M.; Rega, N.; Millam, J. M.; Klene, M.; Knox, J. E.; Cross, J. B.; Bakken, V.; Adamo, C.; Jaramillo, J.; Gomperts, R.; Stratmann,

R. E.; Yazyev, O.; Austin, A. J.; Cammi, R.; Pomelli, C.; Ochterski, J. W.; Martin, R. L.; Morokuma, K.; Zakrzewski, V. G.; Voth, G. A.; Salvador, P.; Dannenberg, J. J.; Dapprich, S.; Daniels, A. D.; Farkas, Ö.; Foresman, J. B.; Ortiz, J. V; Cioslowski, J.; Fox, D. J. Gaussian, Inc., Wallingford CT, 2016.

conditions. (b) EPR spectra of **3a** (0.5 mM in toluene) for $O_2^{\bullet-}$ characterization with 5,5-dimethyl-1-pyrroline-N-oxide (DMPO, 0.3 mM) as the spin-trap reagent in different conditions.
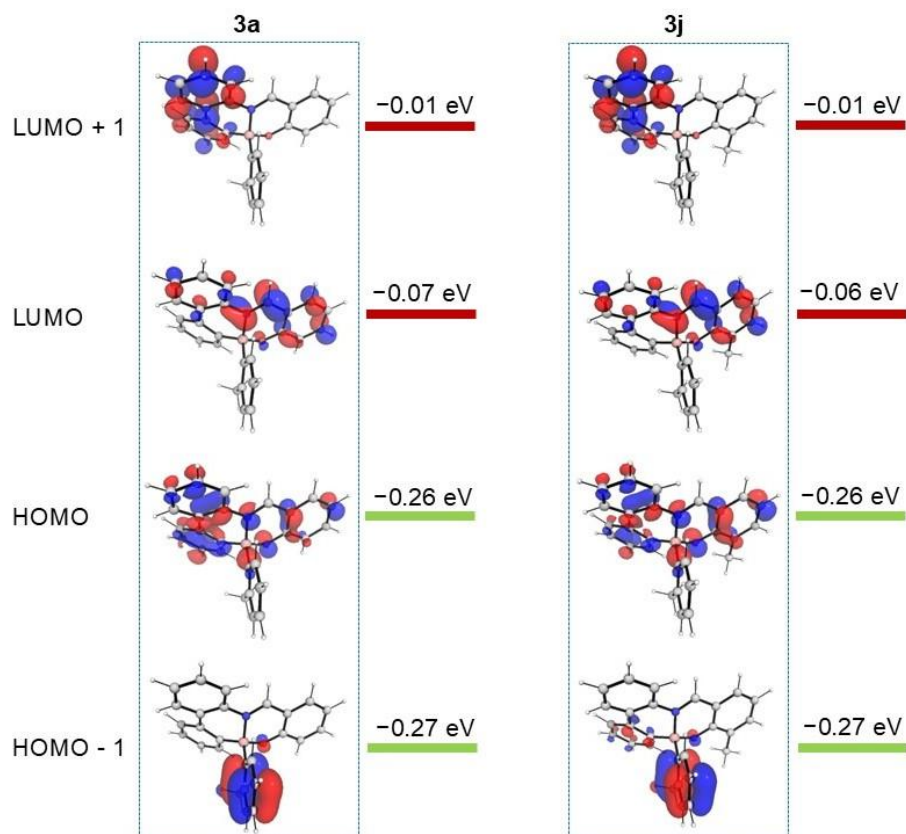
8. Photochemical studies for substrates 3a and 3j

Figure S27. Molecular orbital plots with energy levels for **3a** and **3j** at M06-2X/def2-SVP level of theory.

Table S12. Selected electronic excitation energies (eV) and oscillator strengths (*f*), configurations of the low-lying singlet excited states of **3a** calculated by SMD(toluene)-CAM-B3LYP/def2-TZVPD based on the optimized ground state geometries.

Electronic transition	TD-CAM-B3LYP/def2-TZVPD//M06-2X/def2-SVP			
	Energy/ eV [a]	*f* [b]	Composition [c]	CI [d]
$S_0{\rightarrow}S_1$	3.203 eV 387.1 nm	0.2427	HOMO $\rightarrow$ LUMO	0.8275
$S_0{\rightarrow}S_2$	3.867 eV 320.6 nm	0.0919	HOMO -1 $\rightarrow$ LUMO	0.5957
			HOMO -2 $\rightarrow$ LUMO	0.1820
$S_0{\rightarrow}S_3$	4.282 eV 289.6 nm	0.0220	HOMO -2 $\rightarrow$ LUMO	0.5190
			HOMO -1 $\rightarrow$ LUMO	0.2220

		HOMO -5 → LUMO	0.6621
$S_0 \rightarrow S_4$	4.425 eV 280.2 nm 0.2904	HOMO -3 → LUMO	0.0958
$S_0 \rightarrow S_5$	4.526 eV 274.0 nm 0.0137	HOMO -3 → LUMO	0.5899
		HOMO -2 → LUMO	0.0964

[a] Only the selected low-lying excited states are presented. [b] Oscillator strength. [c] Only the main configurations are presented. [d] The CI coefficients are in absolute values.

Table S13. Selected electronic excitation energies (eV) and oscillator strengths (f), configurations of the low-lying singlet excited states of **3j** calculated by SMD(toluene)-CAM-B3LYP/def2-TZVPD based on the optimized ground state geometries.

Electronic transition	TD-CAM-B3LYP/def2-TZVPD//M06-2X/def2-SVP			
	Energy/ eV [a]	f [b]	Composition [c]	CI [d]
$S_0 \rightarrow S_1$	3.175 eV 390.5 nm	0.2164	HOMO → LUMO	0.8876
$S_0 \rightarrow S_2$	3.863 eV 321.0 nm	0.1297	HOMO -1 → LUMO	0.7228
			HOMO -2 → LUMO	0.1091
$S_0 \rightarrow S_3$	4.326 eV 286.6 nm	0.0228	HOMO -2 → LUMO	0.6114
			HOMO -3 → LUMO	0.1945
$S_0 \rightarrow S_4$	4.341 eV 285.6 nm	0.3439	HOMO -5 → LUMO	0.7810
$S_0 \rightarrow S_5$	4.559 eV 271.9 nm	0.0403	HOMO -3 → LUMO	0.5499
			HOMO → LUMO +1	0.0899

[a] Only the selected low-lying excited states are presented. [b] Oscillator strength. [c] Only the main configurations are presented. [d] The CI coefficients are in absolute values.

Table S14. Vertical singlet and triplet electronic transition energies (in eV) of dyes at the SMD(toluene)-CAM-B3LYP/def2-TZVPD level, along with vertical singlet-triplet splittings (in eV) and the spin-orbit coupling (SOC) values between the involved T_n and S_1 states (in cm^{-1})

Compounds	S_1 (eV)	T_n (eV)	ΔE_{S1-Tn} (eV)	$\langle S_1|\hat{H}SO|T_n\rangle$ (cm^{-1})
3a	3.203	2.314 (T_1)	0.89	0.85
		2.906 (T_2)	0.30	0.69
		3.200 (T_3)	0.003	1.38
3j	3.175	2.301 (T_1)	0.88	0.79
		2.875 (T_2)	0.30	0.53
		3.090 (T_3)	0.09	1.54

References:

(1) Ma, X.; Mai, S.; Zhou, Y.; Cheng, G.-J.; Song, Q. Dual Role of Ethyl Bromodifluoroacetate in the Formation of Fluorine–containing Heteroaromatic Compounds. *Chem. Commun.* **2018**, *54*, 8960–8963.

(2) Marinelli, D.; Fasano, F.; Najjari, B.; Demitri, N.; Bonifazi, D. Borazino-Doped Polyphenylenes. *J. Am. Chem. Soc.* **2017,** *139*, 5503–5519.

(3) Liao, S.; Hu, X.; Li, Y.; Wang, X.; Li, D.; Wang, Q.; Wang, Y.; Huang, X.; Xu, P.; Wu, H.; Li, X.; Yuan, J. Catalyst-free and Eco-friendly Synthesis of Masked Haloarylboronic Acids R (alkyl or aryl) –B(dan) on Water. *Tetrahedron.* **2021**, *90*, 132205–132212.

(4) Inokuma, T.; Takasu, K.; Sakaeda, T.; Takemoto, Y. Hydroxyl Group–Directed Organocatalytic Asymmetric Michael Addition of *α,β*–Unsaturated Ketones with Alkenylboronic Acids. *Org. Lett.* **2009**, *11*, 2425–2428.

(5) Zhao, Y.; Truhlar, D. G. The M06 Suite of Density Functionals for Main Group Thermochemistry, Thermochemical Kinetics, Noncovalent Interactions, Excited States, and Transition Elements: Two New Functionals and Systematic Testing of Four M06-class Functionals and 12 other Functionals. *Theor Chem Account.* **2008**, *120*, 215–241.

(6) Weigend, F.; Ahlrichs, R. Balanced Basis Sets of Split Valence, Triple Zeta Valence and Quadruple Zeta Valence Quality for H to Rn: Design and Assessment of Accuracy. *Phys. Chem. Chem. Phys.* **2005**, *7*, 3297–3305.

(7) Weigend, F. Accurate Coulomb-Fitting Basis Sets for H to Rn. *Phys. Chem. Chem. Phys.* **2006**, *8*, 1057–1065.

(8) Frisch, M. J.; Trucks, G. W.; Schlegel, H. B.; Scuseria, G. E.; Robb, M. A.; Cheeseman, J. R.; Scalmani, G.; Barone, V.; Mennucci, B.; Petersson, G. A.; et al. Gaussian 16, Revision A.01. **2016**.

(9) Marenich, A. V.; Cramer, C. J.; Truhlar, D. G. Universal Solvation Model Based on Solute Electron Density and on a Continuum Model of the Solvent Defined by the Bulk Dielectric Constant and Atomic Surface Tensions. *J. Phys. Chem. B* **2009**, *113*, 6378–6396.

(10) Grimme, S. Supramolecular Binding Thermodynamics by Dispersion-Corrected Density Functional Theory. *Chem.: Eur. J.* **2012**, *18*, 9955–9964.

(11) Funes-Ardoiz, I.; Paton, R. S. GoodVibes v1.0.1 http://doi.org/10.5281/zenodo.56091.

(12) (a) Neese, F. The ORCA program system *Wiley Interdiscip. Rev. Comput. Mol. Sci.*, **2012**, *2*, 73–78. (b) Neese, F. Software update: the ORCA program system -- Version

5.0 *Wiley Interdiscip. Rev. Comput. Mol. Sci.*, **2022**, *12*, *1*, e1606.

(13) Yanai, T.; Tew, D. P.; Handy, N. C. A New Hybrid Exchange–Correlation Functional Using the Coulomb-Attenuating Method (CAM-B3LYP). *Chem. Phys. Lett.* **2004**, *393*, 51–57.

(14) (a) Muniz-Miranda, F.; Presti, D.; Menziani, M. C.; Pedone, A. Electronic and optical properties of the Au_{22}[1,8-bis(diphenylphosphino)octane]$_6$ nanoclusters disclosed by DFT and TD-DFT calculations. *Theor. Chem. Acc.* **2016**, *135*, 5. (b) Muniz-Miranda, F.; Menziani, M. C.; Pedone, A. DFT and TD-DFT Assessment of the Structural and Optoelectronic Properties of an Organic−Ag_{14} Nanocluster. *J. Phys. Chem. A* **2015**, *119*, 5088−5098. (c) Wobbe, M. C. C.; Kerridge, A.; Zwijnenburg, M. A. Optical excitation of MgO nanoparticles; a computational perspective. *Phys. Chem. Chem. Phys.* **2014**, *16*, 22052–22061. (d) Berardo, E.; Hu, H.-S.; Shevlin, S. A.; Woodley, S. M.; Kowalski, K.; Zwijnenburg, M. A. Modeling Excited States inTiO_2 Nanoparticles: On the Accuracy of a TD-DFT Based Description. *J. Chem. Theory Comput.* **2014**, *10*, 1189–1199. (e) Fihey, A.; Maurel, F.; Perrier, A. Modeling the Absorbance Properties of a Pyrene Chromophore Grafted onto a Au_{25} Nanocluster: A TD-DFT Study. *J.Phys. Chem. C* **2014**, *118*, 4444−4453. (f) Rabilloud, F. Assessment of the Performance of Long-Range-Corrected Density Functionals for Calculating the Absorption Spectra of Silver Clusters. *J. Phys. Chem. A* **2013**, *117*, 4267–4278. (g) Stauber, J. M.; Schwan, J.; Zhang, X.; Axtell, J. C.; Jung, D.; McNicholas, B. J.; Oyala, P. H.; Martinolich, A. J.; Winkler, J. R.; See, K. A.; Miller, T. F.; Gray, H. B.; Spokoyny, A. A Super-Oxidized Radical Cationic Icosahedral Boron Cluster. *J. Am. Chem. Soc.* **2020**, *142*, 30, 12948–12953. (h) Li. B.; Zhang, X.; Stauber, J.; Miller, T. F.; Spokoyny, A. Electronic Structure of Super-Oxidized Radical Cationic Dodecaborate-Based Clusters. *J. Phys. Chem. A.* **2021**, *125*, 28, 6141–6150.

(15) Contreras-García, J.; Johnson, E. R.; Keinan, S.; Chaudret, R.; Piquemal, J. P.; Beratan, D. N.; Yang, W. NCIPLOT: A Program for Plotting Noncovalent Interaction Regions. *J. Chem. Theory Comput.* **2011**, *7*, 625–632.

(16) Schrödinger, L. *The PyMOL Molecular Graphics Development Component, Version 1.8*; **2015**.

(17) (a) Pathak, T. P.; Sigman, M. S. Applications of Ortho-Quinone Methide Intermediates in Catalysis and Asymmetric Synthesis. *J. Org. Chem.* **2011**, *76*, 9210-9215. (b) Willis, N. J.; Bray, C. D. Ortho-Quinone Methides in Natural Product Synthesis. *Chem. Eur. J.* **2012**, *18*, 9160–9173.

(18) Zhang, G.; Cai, X.; Jia, J.; Feng, B.; Yang, K.; Song, Q. Cu(I)-Catalyzed Highly Diastereo- and Enantioselective Constructions of Boron / Carbon Vicinal Stereogenic Centers *via* Insertion Reaction. *ACS Catal.* **2023**, *13*, 9502–9508.

(19) Höpfl, H. The Tetrahedral Character of the Boron Atom Newly Defined-A Useful Tool to Evaluate the N→B Bond. *J. Organomet. Chem.* **1999**, *581*, 129–149.

(20) Zu, B.; Guo, Y.; He, C. Catalytic Enantioselective Construction of Chiroptical Boron Stereogenic Compounds. *J. Am. Chem. Soc.* **2021**, *143*, 16302–16310.

(21) (a) Rana, A.; and Panda, P. β-Octamethoxyporphycenes. *Org. Lett.* **2014**, *16*, 78-81. (a) Shimakoshi, H.; Baba, T.; Iseki, Y.; Aritome, I.; Endo, A.; Adachi, C.; Hisaeda, Y. *Chem. Commun.* **2008**, 2882-2884. (b) Shao, W.; Wang, H.; He, S.; Shi, L.; Peng, K.; Lin, Y.; Zhang, L.; Ji, L.; Liu, H. *J. Phys. Chem. B* **2012**, *116*, 14228-14234. (c) Rubio, N.; Prat, F.; Bou, N.; Borrell, J. I.; Teixido, J.; Vollanueva, A.; Juarranz, A.; Canete, M.; Stockert, J. C.; Nonell, S. *New J. Chem.* **2005**, *29*, 378-384. A_2B-and A_3-type Boron (III) Subchlorins Derived from Meso -diethoxycarbonyltripyrrane:synthesis and Photophysical Exploration. (d) Arnbjerg, J.; Jiménez-Banzo, A.; Paterson, M. J.; Nonell, S.;Borrell, J. I.; Christiansen, O.; Ogilby, P. R. Two-Photon Absorptionin Tetraphenylporphycenes: Are Porphycenes Better Candidates than Porphyrins for Providing Optimal Optical Properties for Two-Photon Photodynamic Therapy? *J. Am. Chem. Soc.* **2007**, *129*, 5188−5199.